Femtosecond laser nanosurgery
of biological cells and tissues

Alfred VOGEL[*], **Joachim NOACK**[*], **Gereon HÜTTMANN**[*], **Norbert LINZ**[*], **Sebastian FREIDANK**[*],

and Günther PALTAUF[**]

[*] *Biomedizinische Optik, Universität zu Lübeck, Peter-Monnik Weg 4, 23562 Lübeck, Germany*
E-mail: *vogel@bmo.uni-luebeck.de*
[**] *Institut für Physik, Karl-Franzens-Universität, Universitätsplatz 5, A-8010 Graz, Austria*

Femtosecond laser nanosurgery relies on low-density plasma formation followed by chemical effects of the free electrons (bond breaking), thermal effects, and compressive and tensile thermoelastic stress waves that produce transient cavities. We developed models for numerical simulation of these effects and calculated their irradiance thresholds. By comparison of the threshold values to experimentally determined thresholds for various cellular and tissue effects we elucidated the working and damage mechanisms of nanosurgery at kHz and MHz laser repetition rates. By time-resolved detection of the scattering of a cw laser beam we measured the bubble oscillation time and size near the plasma formation threshold for various fs laser wavelengths and numerical apertures of the focusing objective. For NA = 0.9, the smallest bubbles had an oscillation time of 15 ns, corresponding to a radius of 81 nm, in excellent agreement with our theoretical predictions. The bubble dynamics is of interest in the context of transient cell membrane permeabilisation for transfer of genes or other substances into live cells.

Keywords: Femtosecond laser, cell surgery, nanoeffects, plasma, cavitation, thermoelastic stress, transfection, dissection

1. Introduction

Nonlinear absorption of short and ultrashort laser pulses focused through microscope objectives of high numerical aperture (NA) can be used to achieve very fine and highly localized laser effects inside of biological media that are transparent at low irradiance as well as in the bulk of photonic materials [1]. Very large numerical apertures are required both to minimize the diffraction limited focus diameter and to avoid self-focusing and filamentation.

To make use of the full potential of femtosecond pulses for highly localized material processing and modification of biological media, it is essential to understand the underlying mechanisms. We have therefore investigated the evolution of plasma formation and the chemical, thermal, and thermomechanical effects arising from femtosecond optical breakdown in aqueous media. Details about numerical and experimental methods applied in this study can be found in Ref. [1].

2. Plasma formation

While nanosecond breakdown is very abrupt (Figs. 1a, b), we found that in femtosecond laser optical breakdown free electrons are produced in a fairly large irradiance range below the optical breakdown threshold, with a deterministic relationship between free electron density and irradiance (Figs. 1c, d). This provides a large 'tuning range' for the creation of spatially confined chemical, thermal and mechanical effects via free electron generation that can be used for cell surgery. The prediction of low-density plasmas at irradiances below the threshold for bubble formation (Fig. 1d) was experimentally confirmed by Mao et. al. [2].

For larger irradiances, plasmas in bulk media grow beyond the region of the beam waist, which keeps the plasma energy density small. By contrast, at surfaces the energy deposition becomes confined to a thin, dense layer once the free electron density reaches the critical density [3, 4], and the regime of low-density plasma generation has little practical importance.
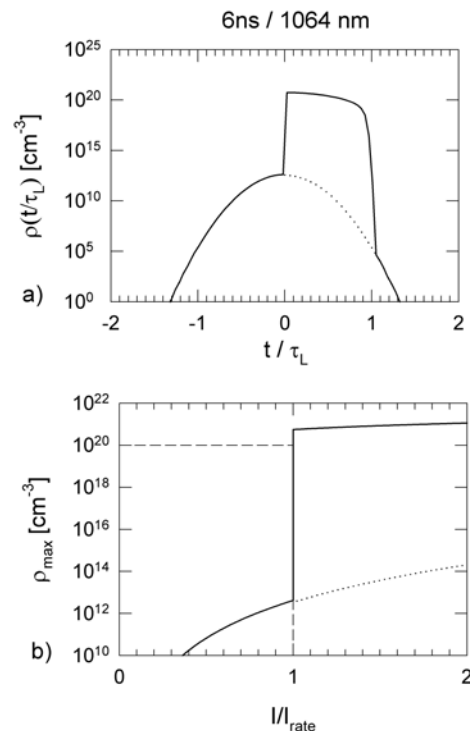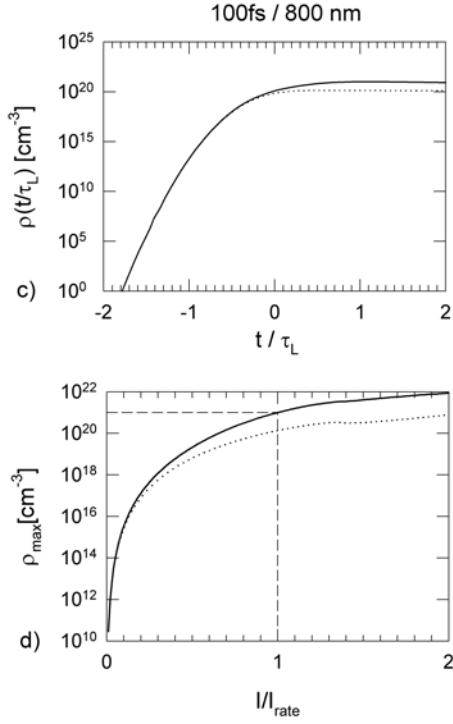
Fig. 1 Evolution of the free-electron density during the laser pulse at the optical breakdown threshold for 6 ns, 1064 nm pulses (a) and for 100-fs, 800-nm pulses (c). The time t is normalized with respect to the laser pulse duration τ_L. The contribution of multiphoton ionization to the total free-electron density is plotted as a dotted line. The maximum free electron density ρ_{max} achieved during the laser pulse as a function of irradiance is, for the same laser parameters, shown in (b) and (d). The irradiance I is normalized with respect to the threshold $I_{rate.} = 10^{21}$ cm^{-3} that is commonly assumed in numerical calculations of the breakdown. The threshold I_{rate} and the corresponding value of ρ_{max} are marked by dotted lines. Reprinted with permission from Ref. [1].

3. Irradiance and free electron distribution within the focal volume

The temperature and stress distribution in the focal region depend on the distribution of quasi-free electrons produced during femtosecond optical breakdown. Therefore, we must explore the shape of the irradiance and free-electron density distributions within the focal volume before we can investigate the resulting temperature and stress effects. For a plane wave focused by a microscope objective, the focal region has an ellipsoidal shape. The short axis d of the ellipsoid is identified with the diameter of the central maximum of the Airy pattern in the focal plane

$$d = 1.22\,\lambda\,/\,NA . \tag{1}$$

The symbol λ refers to the vacuum wavelength of light, and $NA = n_0\,\sin\alpha$ is the numerical aperture of the objective. The ratio l/d of the long and short axes is

$$l\,/\,d = (3 - 2\cos\alpha - \cos 2\alpha)^{1/2}\,/(1-\cos\alpha) \tag{2}$$

for optical setups with very large solid angles [1,5]). Here α is the half angle of the light cone such as used in the definition of the numerical aperture. For NA 1.3, which

in water corresponds to an angle of $\alpha = 77.8°$, we find $l/d = 2.4$ and, for $\lambda = 800$ nm, $d = 750$ nm and $l = 1800$ nm. For our calculations, we approximate the ellipsoidal region of high irradiance in the focus center by a Gaussian distribution, and the boundaries of the ellipsoid are identified with the $1/e^2$ values of this distribution.

When long pulses (µs to ms) are used for cell surgery and energy deposition is based on linear absorption, the possible spatial resolution is related to the temperature distribution in the focal region that is directly related to the irradiance distribution. By contrast, for femtosecond laser pulses, the spatial resolution is defined by the free electron distribution, which, for 800 nm wavelength, is proportional to the 5th power of the irradiance distribution [1]. Due to the nonlinear absorption process underlying optical breakdown, the free-electron distribution is much narrower than the irradiance distribution. For $\lambda = 800$ nm, the diameter of the free -electron distribution at the $1/e^2$- values amounts to 336 nm, the length to 806 nm. Femtosecond-laser nanoprocessing can thus achieve a 2-3 fold better precision than cell surgery using cw irradiation, and enables manipulation at arbitrary locations.

4. Chemical effects of low-density plasmas

The lower end of the irradiance range useful for cell surgery is defined by the regime where the free electron density is still too low to cause any thermal or thermomechanical effects but sufficiently high to cause chemical changes arising from the action of the free electrons. One very important chemical effect is molecular bond breaking that can result from resonant interactions between electrons of 3 -20 eV kinetic energy and biomolecules (Fig. 2) [6].

The irradiance threshold for chemical changes can be assessed using the plot of free-electron density versus irradiance presented in Fig. 1d. At NA = 1.3 and $\lambda = 800$ nm, one free electron per focal volume corresponds to a density of $\rho = 2.1 \times 10^{13}$ cm^{-3}. This value is reached at an irradiance of $I = 0.26 \times 10^{12}$ W cm^{-2} which is 0.04 times the irradiance threshold for breakdown defined as $\rho_c = \rho_{cr} = 10^{21}$ cm^{-3}.

When long oscillator pulse series of $\approx$ 80 MHz repetition rate consisting of 10^4 to 10^6 pulses are employed, their accumulative chemical effects can lead to cell damage and, for larger irradiances, to dissection [1]. According to our calculations, the irradiance required for intranuclear chro-
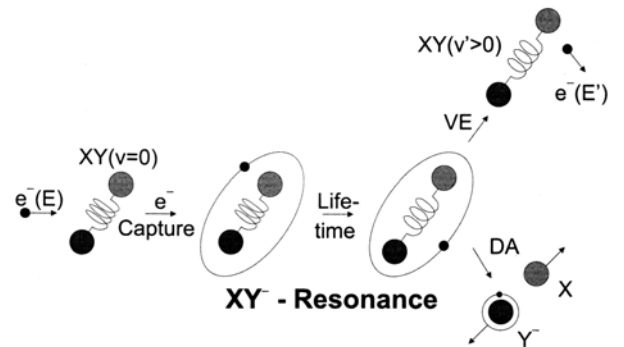

Fig. 2 Dynamics of vibrational excitation and dissociative electron attachment in resonant electron-molecule scattering. Reprinted with permission from Ref. [7].

mosome dissection [8] amounts to 1/6 of the irradiance required to produce $\rho_{cr} = 10^{21}$ cm^{-3}, and about 1000 free electrons per pulse are produced with the parameters used for chromosome dissection [1].

5. Thermal effects

The deposition of laser energy into the medium is mediated by the generation of free electrons. When the energy carried by the free electrons is subsequently transferred to the heavy particles in the interaction volume through collisions and nonradiative recombination, this results in a heating of the atomic, molecular and ionic plasma constituents.

The temperature rise can be determined by calculating the volumetric energy density gained by the plasma during the laser pulse. This calculation is particularly easy for femtosecond pulses because the pulse duration is considerably shorter than the electron cooling and recombination times. Therefore, hardly any energy is transferred during the laser pulse, and the energy density deposited into the interaction volume is simply given by the total number density ρ_{max} of the free electrons produced during the pulse multiplied by the mean energy gain of each electron. The mean energy gain of an electron is, in turn, given by the sum of ionization potential and average kinetic energy. To calculate the temperature rise from the plasma energy density, we assumed that the thermal constants of tissue are equal to those of water. The evolution of the temperature distribution was then calculated by solving the differential equation for heat diffusion [1].

The results are presented in figure 3. They demonstrate that for repetition rates in the MHz range accumulative thermal effects are observed. For 80 MHz, the peak temperature after many pulses is up to 6.8 times higher than after a single pulse for NA = 1.3, and up to 45 times higher for NA = 0.6 (Figs. 3a, b). However, when the repetition rate is reduced to 1 MHz or smaller, heat accumulation disappears even for NA = 0.6 (Fig. 3c) because the narrow free electron distribution, which is the source of the heat deposition, leads to a very rapid heat diffusion.

When laser surgery is performed with 80 MHz pulse series focused at NA = 1.3, the boiling temperature of 100°C will, due to the 6.8-fold temperature accumulation, be reached when each individual pulse produces a temperature rise of 11.8°C (starting from 20°C room temperature). For 800-nm, 100-fs pulses this temperature rise requires a free-electron density of $\rho_c = 2.1 \times 10^{19}$ cm^{-3}, which is reached at an irradiance of 0.51 times the value required for optical breakdown ($\rho_{cr} = 10^{21}$ cm^{-3}).

For NA = 1.3, the heat distribution exhibits a half-width in the submicrometer-range, as shown in Fig. 3d. Thermal effects are thus confined to a very small volume, even for long pulse series for which the thermal distribution resembles that of cw irradiation. However, it needs to be kept in mind that no purely thermal effects can be produced with femtosecond pulses, because due to the nonlinear absorption of the laser light heat generation is always mediated by the production of free electrons. For example, each pulse of a series leading to a final temperature of 100°C (at NA = 1.3) produces $\approx$ 2 Mill. free electrons. The thermal effects are, therefore, always accompanied and probably dominated by free-electron-mediated chemical effects.
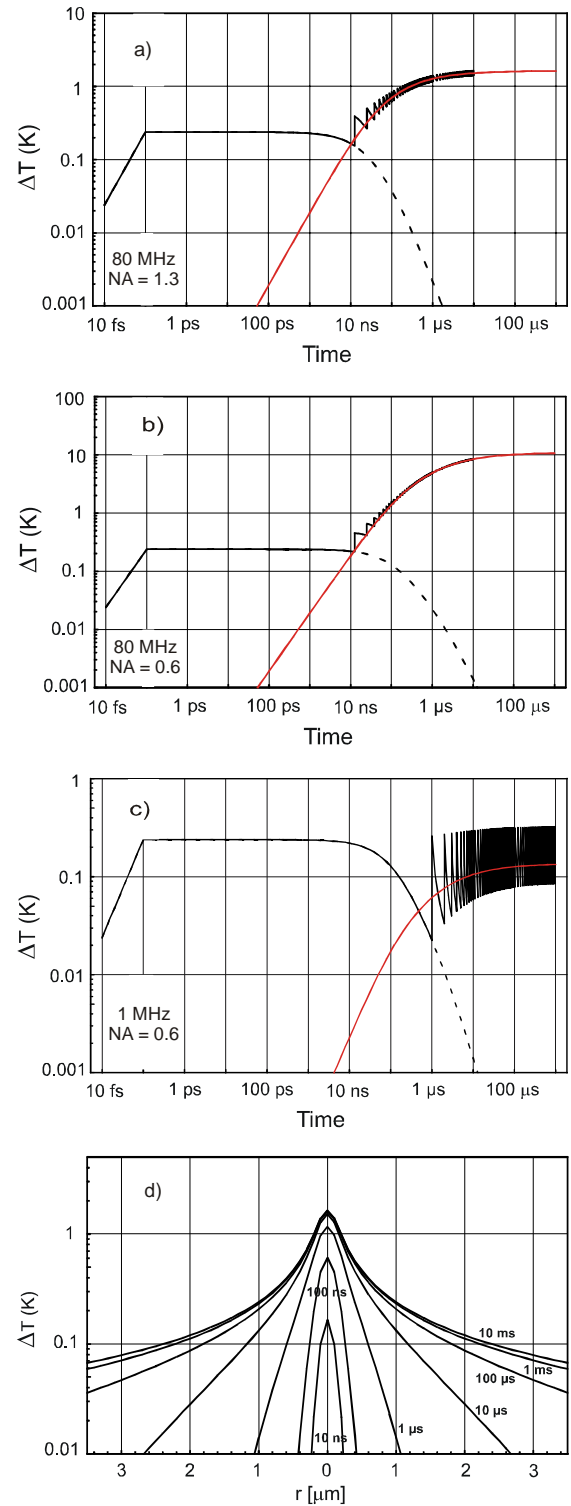

Fig. 3 Temperature evolution at the center of the laser focus produced by a series of 800-nm, 100-fs pulses focused into water (a-c), and the corresponding temperature distribution (d). a) 80 MHz repetition rate, NA = 1.3; b) 80 MHz repetition rate, NA = 0.6; c) 1 MHz repetition rate, NA = 0.6, d) 80 MHz repetition rate, NA = 1.3. The volumetric energy density deposited per pulse was always assumed to be 1 Jcm^{-3} at the focus center. The dashed lines in a) – c) represent the temperature decay after a single pulse. For comparison, the temperature evolution during cw irradiation with the same average power as for pulsed irradiation is also shown. Reprinted from [1].

For even larger irradiances, thermo-mechanical effects (bubble formation) come into play. When bubbles are formed during cell surgery with oscillator pulse series ($\approx$ 80 MHz), they arise from accumulative chemical bond breaking and photothermolysis. They are long lasting, can grow to a fairly large size, and their appearance defines the upper limit of the useful parameter range for cell surgery with oscillator pulse series.

6. Thermoelastic stress evolution

In the single pulse regime $\leq$ 1 MHz, where no temperature accumulation occurs, bubbles are produced by thermo-elastically induced tensile stress. In femtosecond optical breakdown, laser pulse duration and thermalization time of the energy of the free electrons are much shorter than the acoustic transit time from the center of the focus to its periphery. Therefore, no acoustic relaxation is possible during the thermalization time, and the thermo-elastic stresses caused by the temperature rise stay confined in the focal volume, leading to a maximum pressure rise [9, 10]. Conservation of momentum requires that the stress wave emitted from the focal volume must contain both compressive and tensile components such that the integral of the stress over time vanishes. In water or biological cells, the tensile stress wave will cause the formation of a cavitation bubble when the rupture strength of the liquid is exceeded. For cell surgery in the single pulse regime, the threshold for bubble formation defines the onset of disruptive mechanisms contributing to dissection.

To determine the evolution of the thermo-elastic stress distribution in the vicinity of the laser focus, we solved the three-dimensional thermo-elastic wave equation arising from the temperature distribution at the end of a single femtosecond laser pulse [1]. The result is presented in figure 4.

7. Bubble formation

Because the region subjected to large tensile stress amplitudes is very small, the presence of inhomogeneous nuclei that could facilitate bubble formation is unlikely, and we have to consider the tensile strength of pure water to estimate the bubble formation threshold. We use the crossing of the "kinetic spinodal" as defined by Kiselev [11] as threshold criterion for bubble formation. In the thermodynamic theory of phase transitions, the locus of states of infinite compressibility $(\delta p / \delta V)_T = 0$, the spinodal, is considered as a boundary of fluid metastable (superheated) states. Physically, however, the metastable state becomes short-lived due to statistical fluctuations well before the spinodal is reached. The "kinetic spinodal" is the locus in the phase diagram where the lifetime of metastable states becomes shorter than a relaxation time to local equilibrium. For 20°C start temperature, the kinetic spinodal of water is reached at $\Delta T =$ 131.5°C, and $p = -$ 71.5 MPa.

For superthreshold pulse energies, the size of the bubble nucleus was identified with the extent of the region in which the negative pressure exceeds the kinetic spinodal limit. The bubble dynamics was then calculated by means of the Gilmore model, taking the tensile stress around the bubble and the vapor pressure inside the bubble into account as driving forces for the bubble expansion. In these
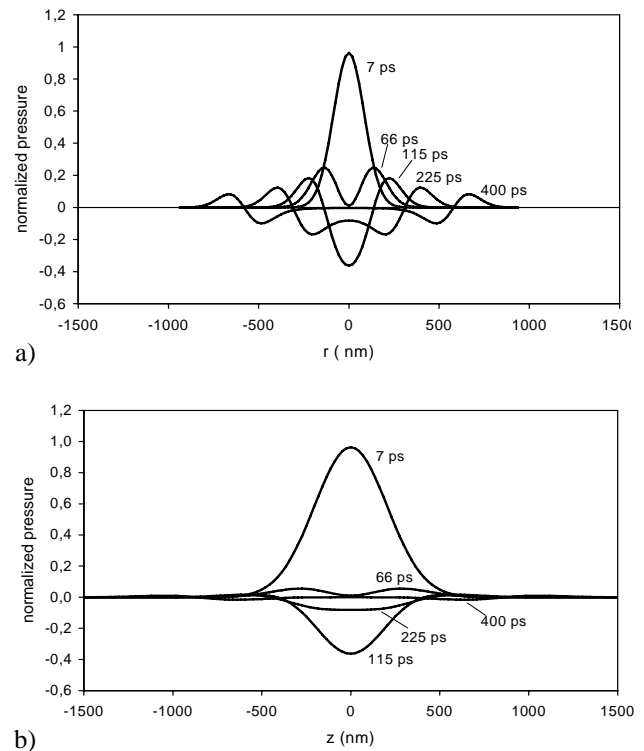
a)

b)

Fig. 4 Stress distribution produced by a single 800-nm, 100-fs pulse focused into water (NA = 1.3). The evolution of the distribution is shown (a) in radial direction, and (b) in axial direction for various times after the release of the laser pulse. The pressure amplitudes are normalized to the peak compressive stress created in the focal volume. Reprinted with permission from Ref. [1].

calculations, we considered the temperature-dependence of the surface tension at the bubble wall. An example for the bubble dynamics after a temperature rise from room temperature to 200°C is given in Fig. 5, and the dependence between maximum bubble size and end temperature is presented in Fig. 6. Our experimental results on stress amplitudes at the bubble formation threshold agree very well with the calculated values, as described in Ref [1].
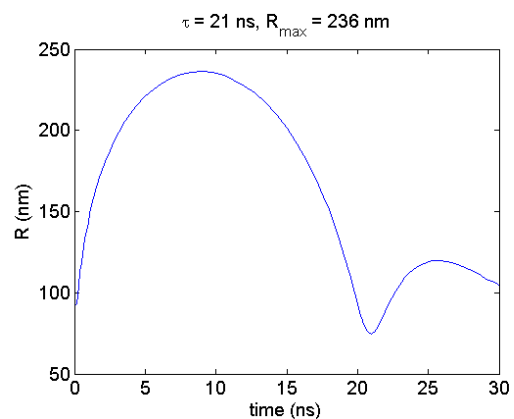
Fig. 5 Calculated radius time curve of the cavitation bubble produced by a single 800-nm, 100-fs laser pulse focused at NA = 1.3 that leads to a peak temperature of T_{max} = 200 °C at the focus center. Isothermal conditions for the bubble content with respect to the surrounding liquid were assumed. Reprinted from [1]
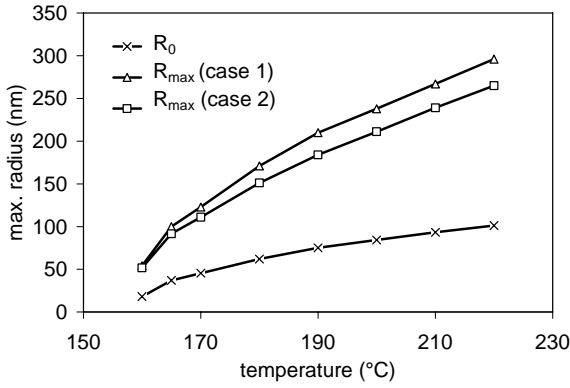
Fig. 6 Maximum bubble radius R_{max} as a function of the peak temperature in the center of the focal volume, together with the radius of the nucleus, R_0. Cases 1 and 2 stand for isothermal and adiabatic conditions for the bubble content with respect to the surrounding liquid. The calculation were pefformed for 800-nm, 100-fs pulses. Reprinted from [1]

The most prominent feature of the transient bubbles produced close to the threshold of femtosecond optical breakdown is their small size and short lifetime. The bubble radius in water right at threshold is as small as 50 nm, and it amounts to about 200 nm for a peak of 200°C temperature in the focus center. The bubbles will be even smaller in a visco-elastic medium such as the cytoplasm. This makes a dissection mechanism associated with bubble formation compatible with intracellular nanosurgery, in contrast to nanosecond optical breakdown where the minimum bubble radius in water observed for NA = 0.9 and λ = 532 nm was R_{max} = 45 µm [12]. The small bubble size corresponds to a small energy of only 53 femtoJoule of the expanded bubble for the case presented in Fig. 5. The smallness of the bubble energy is largely due to the minute energy content of the stress transient creating the bubble. For the case of Fig. 5, the energetic conversion efficiency from heat into the thermo-elastic wave is only 0.46%, and the conversion efficiency from thermo-elastic energy into bubble energy is 6.8%.

The stress-confinement of the energy deposition in femtosecond laser induced material processing results in large compressive and tensile stress amplitudes already after a moderate temperature rise. Therefore, a temperature rise as little as 131.5 °C is sufficient for bubble generation in a liquid without any pre-existing nuclei. The low volumetric energy density required for thermoelastically induced cavity formation, which is only about 1/5 of the vaporization enthalpy, is a reason for the lack of thermal side effects in femtosecond laser dissection and the small conversion rate of laser energy into mechanical energy. Nevertheless, for sufficiently large pulse energies, bubble expansion and shock wave pressure can cause effects far beyond the focal volume that lead to cell death. This is especially important for applications such as optotransfection (transient cell membrane permeabilisation for transfer of genes or other substances into live cells). To avoid unwanted side effects, irradiances should be used that are only slightly above the bubble formation threshold.

8. Experimental determination of breakdown threshold and bubble size

Figure 7 shows a schematic drawing of the experimental setup for our experimental investigations of femtosecond optical breakdown in water at large NA. The laser pulses are generated by an Yb:glass laser system IC-1045-30-fs Reg Amp/SHG/THG (High Q Laser Production). This laser system delivers amplified pulses with 315 fs duration, a center wavelength of λ = 1040 nm, and up to 30 µJ pulse energy at 1 kHz repetition rate. With a combination of two fast shutters (Uniblitz electronics), single pulses can be selected out of the 1 kHz repetition rate signal. The oscillator leakage is suppressed by means of an external pockels cell (Linos LM0202P).

The precise energy adjustment of the pump beam required for a determination of the optical breakdown threshold is achieved by combinations of $\lambda/2$ plates and thin film polarizers, the transmission of which depends on the polarization angle of the incident light. The energy of the laser pulses is measured by diverting a part of the pump beam onto an energy meter (Ophir PD10-pJ).

The calculations in the previous section showed that for optical breakdown at large NA the bubble size expected near threshold is well below the optical resolution limit (Fig. 6). Therefore, a direct photographical observation is impossible. Instead, we used a time-resolved detection of the scattering of a probe laser beam to determine the bubble size via a measurement of its oscillation time. To validate the scattering technique, its results for energies well above the bubble formation threshold were compared with photographically determined bubble sizes.

The core of the setup is a water-filled cuvette with three water immersion microscope objectives built into the cuvette walls that can be confocally adjusted. The cw probe laser beam (658 nm, 25 mW) is aligned collinear with the fs-pump beam and delivered through the focusing objective. The transmitted light is collected by a second microscope objective built into the opposite cell wall. Larger bubbles could be photographed through a third microscope objective (20x) oriented perpendicular to the optical axis of the pump and probe beams.
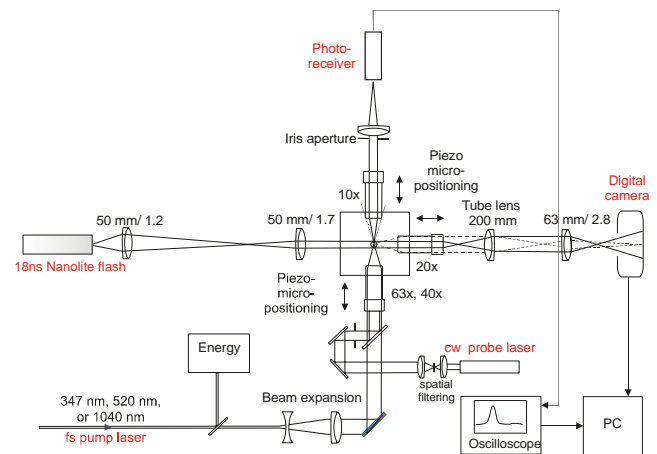

Fig. 7 Setup for the determination of the breakdown threshold and the energy-dependent maximum cavitation bubble size.

5

Axial adjustment for precise focusing and confocal alignment of the three objectives is achieved by piezo-driven micropositioners. When the 40x objective was used to focus the fs-pulses, we could achieve a confocal arrangement with the 20x imaging objective at correct working distance for all objectives. This was not possible with the 63x objective. For illumination of the focal region, we used a Nanolite flash lamp with 18 ns pulse duration. To be able to image very small bubbles near the optical resolution limit, the image formed by the 20x objective and tube lens was further magnified using a Nikkor objective (63mm/1:2,8) that is corrected for 8x magnification. This way, we achieved a total magnification factor of 162.

The scattering signal is detected by an AC-coupled high speed photoreceiver (FEMTO, HCA-S) with a signal bandwidth from 25 kHz to 200 MHz and an additional monitor output of the DC signal that is important for the basic alignment of the entire setup. When the bubble size is much smaller than the focus of the probe laser beam, the scattering signal is much smaller than the total amount of the light transmitted through the focal volume. AC coupling is very useful to remove this bias. The duration of the scattering signal equals the oscillation time of the bubble in the focal volume.

The bubble formation threshold energy was 22.6 nJ for the 40x, NA = 0.8 objective, corresponding to a radiant exposure of 1.15 J/cm^2 averaged over the focal spot.

The maximum bubble radius R_{max} was calculated from the bubble oscillation time T_{osc} using the Rayleigh equation

$$R_{max} = (T_{osc}/1.83)\left[(p_\infty - p_{v_0})/\rho_0\right]^{1/2}, \qquad (3)$$

where p_∞ is the hydrostatic pressure, p_v the vapor pressure inside the bubble, and ρ_0 the mass density of the liquid [13]. Figure 8 shows the results of the probe beam scattering technique, together with the photographically determined values of the bubble size.

For large bubbles, the agreement between the results obtained with both measurement techniques is very good. Close to threshold, the maximum cavitation bubble radius is well below the optical resolution limit and very close to the values predicted by our model calculations (see Fig. 6). However, it must be noted that for bubble sizes close to the optical resolution limit, the 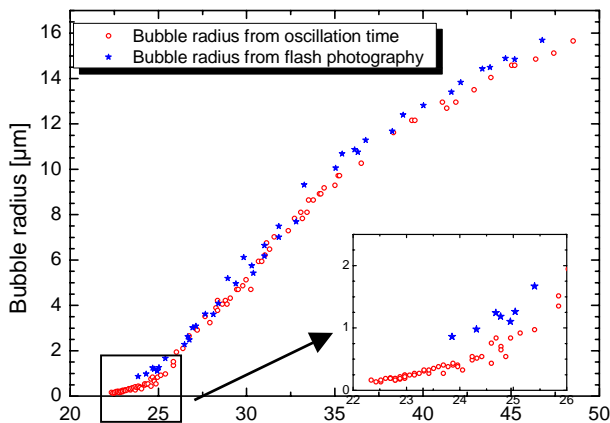Rayleigh equation yields radius values that are considerably smaller than the photographic values. This discrepancy can be explained by the fact that the Rayleigh formula was derived without consideration of surface tension, which exerts a pressure $p = 2\sigma/R$ in addition to the hydrostatic pressure. The pressure by surface tension can be neglected for large bubbles but becomes important for bubble radii of a few µm or below. In water at room temperature, the surface tension against air is 0.073 N/m, and the corresponding pressure acting on bubbles of for example 100 nm radius is 1.46 MPa. Since this value is much larger than the hydrostatic pressure of 0.1 MPa, surface tension will considerably alter the relationship between bubble oscillation time and maximum radius. It will shorten the oscillation time for a given radius and, vice versa, the actual radius for a measured oscillation time will be larger than the radius predicted by Eq. (3).

9. Implications for laser effects on cells and tissues

An overall view of physical effects induced by femtosecond laser pulses in comparison to experimental data on cell surgery is given in figure 9. It allows to assess the working mechanisms in the different regimes of nanosurgery. Dissection at 80 MHz repetition rate is performed in the low-density plasma regime at pulse energies well below the optical breakdown threshold. It is mediated by free-electron-induced chemical decomposition (bond breaking) in conjunction with multiphoton-induced chemistry, and not related to heating or thermo-elastic stresses. When the energy is raised, long-lasting bubbles are produced by accumulative heating and tissue dissociation into volatile fragments that are usually unwanted. By contrast, dissection with 1 kHz repetition rate is performed using about 10-fold larger pulse energies and relies on thermo-elastically-induced formation of minute transient cavities with life times < 100 ns.
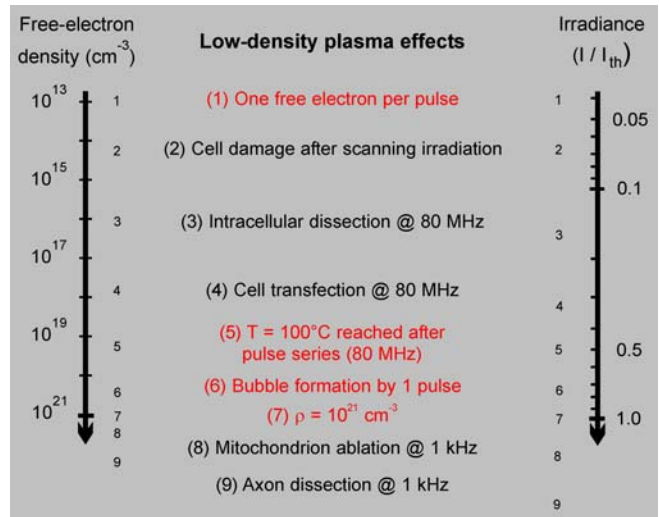
Fig. 9 Overall view of physical breakdown phenomena induced by femtosecond laser pulses, together with experimental damage, transfection and dissection thresholds on cells, scaled by free-electron density and irradiance. The irradiance values are normalized to the optical breakdown threshold I_{th} defined by $\rho_{cr} = 10^{21}$ cm^{-3}. All data refer to plasma formation in water with femtosecond pulses of about 100 fs duration and 800 nm wavelength. Reprinted from [1].

Fig. 8 Bubble radius determined by photography and probe beam scattering. 40x objective, NA = 0.8, λ = 1064 nm.

Both modes of fs-laser nanoprocessing can achieve a 2-3 fold better precision than cell surgery using cw irradiation (see section 3) and enable manipulation at arbitrary locations [1].

Besides for nanoprocessing of biological materials, femtosecond laser induced plasmas can also be used to modify other transparent materials and enable the generation of photonic elements in bulk glass and fused silica. The process of plasma generation and void formation in the bulk of dielectrica like fused silica and glass resembles the process in water, and the methods developed in our study can also be applied to solid dielectrica. However, differences in the band gap energy and material properties will lead to somewhat larger threshold values for chemical and thermomechanically induced changes in solids compared to aqueous media.

References

[1] A. Vogel, J. Noack, G. Hüttman, and G. Paltauf: Mechanisms of femtosecond laser nanosurgery of cells and tissues. *Appl. Phys. B* **81** (2005) 1015.

[2] S. S. Mao, F. Quéré, S. Guizard, X. Mao, R.E. Russo G. Petite, and P. Martin: *Appl. Phys. A* **79** (2004) 1695.

[3] B. C. Stuart, M.D. Feit, S. Hermann, A.M. Rubenchik, B.W. Shore, and M.D. Perry: *Phys. Rev. B* **53** (1996) 1749.

[4] A.P. Joglekar, H. Liu, E. Meyhöfer, G. Mourou, and A.L. Hunt: *Proc. Nat. Acad. Sci.* **101** (2004) 5856.

[5] S. Grill, and E. H. K. Stelzer: *J. Opt. Soc. Am. A* **16** (1999) 2658.

[6] B. Boudaiffa, P. Cloutier, D. Hunting, M.A. Huels, and L. Sanche: *Science* **287** (2000) 1658.

[7] H. Hotop: "Proceedings of the International Symposium on Gaseous Dielectrics," ed. by L.G. Christophorou and J.K. Olthoff (Kluwer Academic/Plenum, New York, 2001) p. 3.

[8] K. König, I. Riemann, P. Fischer, and K. Halbhuber: *Cell. Mol. Biol.* **45** (1999) 195.

[9] A. Vogel, and V. Venugopalan: *Chem. Rev.* **103** (2003) 577.

[10] G. Paltauf, and P. Dyer: *Chem. Rev.* **103**, (2003) 487.

[11] S.B. Kiselev: *Physica A* **269** (1999) 252.

[12] V. Venugopalan, A. Guerra, K. Nahen, and A. Vogel: *Phys. Rev. Lett.* **88**, (2002) 078103.

[13] L. Rayleigh: *Philos Mag* **34** (1917) 94-98